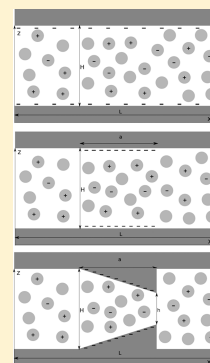


# Charge Transport in Nanochannels: A Molecular Theory

Umberto Marini Bettolo Marconi<sup>\*,†</sup> and Simone Melchionna<sup>\*,‡</sup><sup>†</sup>Scuola di Scienze e Tecnologie, Università di Camerino, Via Madonna delle Carceri, 62032 Camerino, INFN Perugia, Italy<sup>‡</sup>CNR-IPCF, Consiglio Nazionale delle Ricerche, P.le A. Moro 2, 00185 Rome, Italy

**ABSTRACT:** We introduce a theoretical and numerical method to investigate the flow of charged fluid mixtures under extreme confinement. We model the electrolyte solution as a ternary mixture comprising two ionic species of opposite charge and a third uncharged component. The microscopy approach is based on kinetic theory and is fully self-consistent. It allows us to determine configurational properties, such as layering near the confining walls and the flow properties. We show that, under the appropriate assumptions, the approach reproduces the phenomenological equations used to describe electrokinetic phenomena, without requiring the introduction of constitutive equations to determine the fluxes. Moreover, we model channels of arbitrary shape and nanometric roughness, features that have important repercussions on the transport properties of these systems. Numerical simulations are obtained by solving the evolution dynamics of the one-particle phase-space distributions of each species by means of a lattice Boltzmann method for flows in straight and wedged channels. Results are presented for the microscopic density, the velocity profiles, and the volumetric and charge flow rates. Strong departures from electroneutrality are shown to appear at the molecular level.



## 1. INTRODUCTION

Understanding the motion of electrical charges in liquid solutions is at the core of many recent advances in biological and technological applications, including molecular separation processes, DNA sequencing, oil recovery, decontamination of soils by extracting and removing pollutants and toxins, manipulation of colloidal materials, and so forth. Electro-nanofluidics allows us to control the movement of liquids in and around objects with characteristic size  $H$  on the order of 10–50 nm and requires a deep understanding of the transport properties of small amounts of fluids.<sup>1–3</sup> In fact, charged liquid solutions under confinement behave in a distinctive way under the influence of electric fields because their flow properties depend on the charges of the moving ions and on those sitting at the pore walls. An ionic atmosphere charged oppositely with respect to the surface charge with a thickness proportional to the Debye length,  $\lambda_D$ , forms next to the walls, giving rise to the so-called electric double layer (EDL). The difference with neutral fluids is more pronounced when the Debye screening length of the mobile charges becomes comparable to the size of the confining pores.<sup>4,5</sup>

Smoluchowski provided the first explanation of mass transport of electrolytes in electro-osmotic conduits by using the theory of the EDL of Gouy and Chapman. He computed the electric field due to both the surface charges and the mobile ions by solving the Navier–Stokes (NS) equation in the limit of small Reynolds numbers. In electrically driven flows, the predicted fluid velocity profile of an electrolyte displays a characteristic pluglike profile departing from the Poiseuille parabolic profile observed in pressure-driven fluids.<sup>6</sup> The work of Nernst and Planck, instead, extended the standard theory of diffusion to include ionic systems by representing the ionic current in terms of a phenomenological convection–diffusion–migration equation.<sup>7</sup>

Although successful in describing microfluidic phenomena, the classical electrokinetic approach fails to represent the behavior of a nanoscopic system. Its major shortcoming is the continuum description, which breaks down on atomistic scales where the system behavior becomes dominated by wall effects and it is even hard to define a bulk volume. Whereas in microfluidics the effect of the surface charge affects the fluid only within a distance on the order of  $\lambda_D \ll H$ , in nanochannels the Debye length may cause the channel to become ion-selective by excluding one type of ion over another.<sup>8</sup> Therefore, some features of the continuum approach have to be modified (a) by considering the molecular nature of the solvent that competes for room in the pores and affects the structural properties of the EDL and (b) by treating the transport properties beyond the standard NS and Poisson–Nernst–Planck (PNP) equations that are valid in the hydrodynamic limit.<sup>9</sup>

A variety of methods in statistical mechanics have been applied to study the transport and structural properties of charged fluids from a microscopic perspective. These methods include molecular dynamics (MD) simulations,<sup>10</sup> density functional theory in conjunction with the Navier–Stokes equation,<sup>11</sup> and an energy-variational method.<sup>12</sup> Among these, the nonequilibrium MD technique<sup>13</sup> provides in principle the best description that is subject to fewer approximations than other methods. However, in the case of electrokinetic flows it has to cope with two kinds of difficulties: (a) in the systems of interest, the ion concentrations can be orders of magnitude lower than the solvent concentration so that statistical accuracy is reached only at the expenses of long computer runs and (b) the electro-osmotic speeds are much

Received: March 16, 2012

Revised: August 20, 2012

Published: August 23, 2012

slower than the thermal speed, rendering it difficult to extract the signal from the background noise.

The density functional approach of Griffith and Nilson<sup>11</sup> deals rather accurately and microscopically with the configurational description of a ternary system describing an assembly of positive and negative ions immersed in a sea of hard sphere dielectric particles mimicking water molecules but resorts to a macroscopic treatment of the fluid velocity introduced by means of a Navier–Stokes equation, thus neglecting the local dependence of the transport coefficient on the density fluctuations. The energy variational treatment of ions in protein channels is similar in spirit, although derived from different premises, but considers only a primitive electrolyte model; that is, the solvent is not dealt with explicitly.<sup>12</sup> For complex pore geometries of physical interest, one usually resorts to numerical tools such as the finite element method, finite difference, boundary element,<sup>14</sup> spectral techniques,<sup>15</sup> and, recently, lattice Boltzmann methods,<sup>16–21</sup> to mention just a few.

In this article, we propose a treatment for structural and dynamical aspects of electrokinetics in confined ionic systems by an extension of the nonlocal Boltzmann–Enskog equation<sup>22</sup> recently developed by us for neutral multicomponent mixtures. The method requires a knowledge of the inhomogeneous microscopic pair correlation functions of the fluid and in principle accommodates the same level of microscopic detail as the dynamical density functional theory.<sup>23–25</sup> The advantage of the present approach is that both the equilibrium and nonequilibrium forces (which determine the transport coefficients) are derived from the same principle. Thus, we are able to predict not only the density profiles of each species but also the velocity profiles without resorting to further approximations. In practice, the method brings together molecular aspects (microscopic structure, nonideal gas effects in the equation of state, and microscopically determined transport coefficients) with hydrodynamic aspects of correlated fluids.

Our theory employs an approximate method, as introduced about 20 years ago by Dufty and co-workers,<sup>26,27</sup> to reduce the complexity of the full collision operator to a form amenable to fast iterative numerical solutions. This approximation is based on the idea of separating the fast degrees of freedom, giving a minor contribution to the transport properties, from the slow hydrodynamic modes, which on the contrary are very relevant. By this strategy, one achieves a considerable simplification of the resulting kinetic equations with respect to the original Enskog–Boltzmann equations. This set of equations represents the interactions as self-consistent nonlocal forces and is amenable to numerical solution. In the past, numerical solutions of the Boltzmann–Enskog equation for inhomogeneous systems were prevented by the difficulty of solving for the distribution function in the 7D phase space. This obstacle, however, can be overcome by following the same strategy introduced by us to handle neutral systems under inhomogeneous conditions. We have shown that a numerical solution method can be obtained in the framework of the lattice Boltzmann approach.<sup>28–32</sup>

The structure of this article is the following. In Section 2, we prepare the scene by briefly summarizing the phenomenological transport equations for the mass and charge transport in pores. In Section 3, we set up the necessary formalism, based on an extension of the Enskog–Boltzmann transport equation, to deal with a ternary mixture comprising positively and negatively charged hard spheres to simulate the ions and uncharged hard spheres for the solvent. Next, by projecting the transport equations onto the hydrodynamic space, we formally recover the same structure of equations for the

charge, the mass, and the momentum as the phenomenological model. We then obtain a microscopic expression of all the transport coefficients and include nonideal gas effects in the theory. We extract qualitative predictions from our theory and finally present solutions of the full coupled system of transport equations using the LBE method. In Section 4, we discuss how to solve the governing transport equations numerically by means of a lattice technique that bypasses the problem of solving the density and momentum equations separately. After validating the numerical method using some known results, we have made some applications to show its capability to predict the conductance and the volumetric flows in a series of nonuniform channels. In Section 6, we make some conclusive remarks and considerations.

## 2. MODEL SYSTEM

The model considered here treats the electrolyte solution as a ternary mixture. Positively and negatively charged hard spheres with pointlike charges located at their centers represent counter ions and co-ions, whereas neutral spheres represents the solvent.<sup>33</sup> Each species, denoted by  $\alpha$ , has mass  $m^\alpha$ , diameter  $\sigma^{\alpha\alpha}$ , and charge  $z^\alpha e$ , with  $e$  being the proton charge and  $z^\alpha$  being the ion valence. The index  $\alpha = 0$  identifies the solvent whose valence is zero, and  $\alpha = \pm$  identifies the two oppositely charged ionic species. The particles are immersed in a medium of constant and uniform dielectric permeability,  $\epsilon$ , and mutually interact via the potential

$$U^{\alpha\beta}(r) = \begin{cases} \frac{z^\alpha z^\beta e^2}{\epsilon r} & \text{if } r \geq \sigma^{\alpha\beta} \\ \infty & \text{if } r < \sigma^{\alpha\beta} \end{cases} \quad (1)$$

The nonCoulombic part of the interaction is represented by an infinite repulsion that prevents the centers of any two particles from getting closer than the distance  $\sigma^{\alpha\beta} = (\sigma^{\alpha\alpha} + \sigma^{\beta\beta})/2$ . We shall not consider other types of interactions such as attractive solvation forces between ions and solvent, which can be important to stabilize the solution.<sup>13</sup>

In the kinetic description employed here, repulsive forces are accounted for by means of instantaneous collisions and treated a la Enskog, and the remaining forces are treated within the random phase approximation, disregarding correlations. Our treatment neglects the excess free energy stemming from electrostatic correlations, an approximation that can be justified by assuming that it is small compared to the excess free energy associated with the excluded volume term.

We first define the basic variables of our theory. Given the partial number densities  $n^\alpha(\mathbf{r}, t)$ , the total number density is

$$n(\mathbf{r}, t) = \sum_{\alpha} n^\alpha(\mathbf{r}, t) \quad (2)$$

the charge density  $\rho_e(\mathbf{r}, t)$  of the fluid is

$$\rho_e(\mathbf{r}, t) = e \sum_{\alpha} z^\alpha n^\alpha(\mathbf{r}, t) \quad (3)$$

and the total mass density is

$$\rho_m(\mathbf{r}, t) = \sum_{\alpha} m^\alpha n^\alpha(\mathbf{r}, t) \quad (4)$$

We also define the average velocities of each species,  $\mathbf{u}^\alpha(\mathbf{r}, t)$ , and the average barycentric velocity as

$$\mathbf{u}(\mathbf{r}, t) = \frac{\sum_{\alpha} m^\alpha n^\alpha(\mathbf{r}, t) \mathbf{u}^\alpha(\mathbf{r}, t)}{\rho_m(\mathbf{r}, t)} \quad (5)$$

In the following, we neglect spatiotemporal variations of the temperature,  $T$ , for the sake of simplicity.

**2.1. Continuum Equations.** Before proceeding with the microscopic treatment, it is worth reviewing the macroscopic description of the transport of charged liquids. Even the simplest theoretical description of electrokinetic phenomena requires the use of three physical models: (a) the Poisson equation relating the electric field to its source, the spatial charge distribution; (b) the constitutive Nernst–Planck equation giving the current of each ionic species as a function of fluid velocity, charge distribution, and applied electric field; (c) the hydrodynamic continuity and Navier–Stokes (NS) equations relating the density and fluid velocity to the body and pressure forces acting on the system.

The three equations are coupled, and their solution can be obtained by standard numerical methods.<sup>6</sup> Because of its low computational cost, the Poisson–Nernst–Planck equation represents the workhorse for diffusive electrokinetic phenomena.<sup>7</sup> It treats the ions as point particles mutually interacting via the Coulomb potential and experiencing a drag force stemming from the solvent. The solvent does not explicitly enter the description but determines only the values of the dielectric constant and those of the transport coefficients.

The ionic currents,  $\mathbf{J}^\pm \equiv n^\pm \mathbf{u}^\pm$ , have the following phenomenological Nernst–Planck expression

$$\mathbf{J}^\pm(\mathbf{r}, t) = -D^\pm \nabla n^\pm(\mathbf{r}, t) - \lambda^\pm e z^\pm n^\pm(\mathbf{r}, t) \nabla \psi(\mathbf{r}, t) + n^\pm(\mathbf{r}, t) \mathbf{u}(\mathbf{r}, t) \quad (6)$$

which is the superposition of three contributions: (i) the one proportional to the gradient of the ionic concentration via the diffusion coefficient,  $D^\pm$ , (ii) the migration current proportional to the gradient of the electrostatic potential  $\psi(\mathbf{r}, t)$  via the Nernst–Einstein mobility  $\lambda^\pm = D^\pm/(k_B T)$ , on account of the friction exerted by the solvent on the ions, (iii) and the convective current due to the displacement of the fluid with velocity  $\mathbf{u}$ . In the Nernst–Planck approximation, the cross coefficients that couple the diffusive transport of the different components are neglected. In the Stefan–Boltzmann approach, instead such a coupling is preserved, but the determination of the cross-coefficients requires either a detailed microscopic theory or careful experimentation.<sup>9</sup>

The electrostatic potential  $\psi(\mathbf{r}, t)$  is generated by the charge distribution  $\rho_e(\mathbf{r}, t)$  and by the fixed charges located on the pore surfaces and on the electrodes and satisfies the Poisson equation

$$\nabla^2 \psi(\mathbf{r}, t) = -\frac{\rho_e(\mathbf{r}, t)}{\epsilon} \quad (7)$$

with boundary conditions  $-\nabla \psi(\mathbf{r}, t) = \Sigma(\mathbf{r})/\epsilon$  at the confining surfaces, where  $\Sigma(\mathbf{r})$  is the surface charge density. The Poisson–Nernst–Planck (PNP) equation is obtained by considering the local conservation law

$$\frac{\partial}{\partial t} n^\pm(\mathbf{r}, t) + \nabla \cdot \mathbf{J}^\pm(\mathbf{r}, t) = 0 \quad (8)$$

with  $\mathbf{J}^\pm$  given by eq 6 and  $\psi$  given by the Poisson equation (eq 7). To complete the picture, one determines the velocity by considering the Navier–Stokes evolution equation for  $\mathbf{u}(\mathbf{r}, t)$

$$\partial_t \mathbf{u} + \mathbf{u} \cdot \nabla \mathbf{u} = -\frac{1}{\rho_m} \nabla P + \frac{\rho_e}{\rho_m} \mathbf{E} + \frac{\eta}{\rho_m} \nabla^2 \mathbf{u} + \frac{\frac{1}{3}\eta + \eta_b}{\rho_m} \nabla(\nabla \cdot \mathbf{u}) \quad (9)$$

where  $P$  is the hydrostatic pressure,  $\eta$  and  $\eta_b$  are the shear and bulk dynamic viscosities, respectively, and  $\mathbf{E}$  is the electric field, which is the sum of the field due to the ions and the external charges.

When considering a laminar flow in a straight slitlike channel, normal to the  $z$  direction, by imposing the vanishing of the current in the  $z$  direction in eq 6 one obtains the Boltzmann ionic distribution along  $z$ :  $n^\pm(z) = c^\pm e^{-e z^\pm \psi(z)/k_B T}$ , where  $\psi(z)$  is determined with the help of eq 7. The constants  $c^\pm$  are fixed by boundary conditions, as discussed below.

The stationary solutions of eq 9 are of great interest when the electrolytes are driven through narrow channels by an external electric field. Since the pioneering work of Smoluchowski on electro-osmotic phenomena, it is known that when  $\lambda_D \ll H$  the velocity is independent of the conduit size  $H$ , unlike pressure-driven flows. This fact is very important and makes it convenient to use electric driving to pump fluids in ultrafine capillaries. In nanometric channels, this condition is hardly realized.

For vanishing pressure gradients and under creeping flow conditions (Stokes approximation), one can again use eq 7 to eliminate the charge density  $\rho_e$  and obtain from eq 9 the following relation between the fluid velocity and the externally imposed electric field along the  $x$  direction

$$\epsilon E_x \frac{\partial^2 \psi(z)}{\partial z^2} = \eta \frac{\partial^2 u_x(z)}{\partial z^2} \quad (10)$$

with  $E_x = (-\partial/\partial_x)\psi$ . By imposing the condition of vanishing velocity at the surfaces of the channel, located at  $z = 0$  and  $z = H$ , one finds the celebrated Smoluchowski relation

$$u_x(z) = (\psi(z) - \zeta) \frac{\epsilon E_x}{\eta} \quad (11)$$

where  $\zeta$  is the value of the potential at the shear plane where the velocity vanishes.<sup>5</sup>

The main drawback of the macroscopic approach is that it holds only if the ions are treated as pointlike particles migrating under the action of the self-induced electric field, diffusing in the solvent and convected by the flowing solvent. When transport occurs through narrow channels, the deviation from this ideal gas representation becomes crucial.

### 3. MICROSCOPIC APPROACH

In the following text, we shall introduce a microscopic representation of the electrolytic solution by switching to a kinetic description. We will extend the self-consistent dynamical method, which we recently employed to study neutral binary mixtures, to ternary charged mixtures. We consider the following set of Enskog-like equations governing the evolution of the one-particle phase space distributions  $f^\alpha(\mathbf{r}, \mathbf{v}, t)$  of each species:

$$\begin{aligned} \frac{\partial}{\partial t} f^\alpha(\mathbf{r}, \mathbf{v}, t) + \mathbf{v} \cdot \nabla f^\alpha(\mathbf{r}, \mathbf{v}, t) + \frac{\mathbf{F}^\alpha(\mathbf{r})}{m^\alpha} \cdot \frac{\partial}{\partial \mathbf{v}} f^\alpha(\mathbf{r}, \mathbf{v}, t) \\ = \sum_\beta \Omega^{\alpha\beta}(\mathbf{r}, \mathbf{v}, t) \end{aligned} \quad (12)$$

The left-hand side of eq 12 represents the streaming contribution to the evolution, with  $\mathbf{F}^\alpha$  being the external force acting on species  $\alpha$  and merely reflects the Liouville-like single-particle dynamics whereas the right-hand side involves the interactions among the particles and will be the object of a series of approximations in order to render the theory numerically tractable. The first approximation<sup>31</sup> consists of separating the

interaction into a harshly repulsive term, whose effect is represented as collisions between hard spheres, and terms whose gradients have a slower spatial variation and can be treated within a mean-field-like approximation. According to the Enskog approach, the effect of repulsion is obtained by considering pairs of particles dynamically uncorrelated before collisions, but with probabilities modulated by the static pair distribution function. The velocities of these pairs, however, emerge as correlated after a collision. The collision process is described within the revised Enskog theory (RET) proposed by van Beijeren and Ernst,<sup>22</sup> which is known to give good results for the transport properties of hard spheres. Because even the RET operator  $\Omega^{\alpha\beta}$  (see ref 32 for an explicit representation) is awkward to manage, simplifying methods are very convenient: the RET operator is further simplified by invoking the approximation put forward by Dufty and co-workers,<sup>26,27</sup> which separates the hydrodynamic from the nonhydrodynamic contributions to  $\Omega^{\alpha\beta}$  and employs a projection technique. By extending such a prescription to the present case, we obtain

$$\begin{aligned} \sum_{\beta} \Omega^{\alpha\beta}(\mathbf{r}, \mathbf{v}, t) \approx & -\omega[f^{\alpha}(\mathbf{r}, \mathbf{v}, t) - \phi_{\perp}^{\alpha}(\mathbf{r}, \mathbf{v}, t)] \\ & + \frac{\Phi^{\alpha}(\mathbf{r}, t)}{k_{\text{B}}T} \cdot (\mathbf{v} - \mathbf{u}(\mathbf{r}, t)) \phi^{\alpha}(\mathbf{r}, \mathbf{v}, t) \\ & - \frac{e z^{\alpha}}{m^{\alpha}} \nabla \psi(\mathbf{r}) \cdot \frac{\partial}{\partial \mathbf{v}} f^{\alpha}(\mathbf{r}, \mathbf{v}, t) \end{aligned} \quad (13)$$

The term  $\Phi^{\alpha}$  represents the sum of the internal forces of a nonelectrostatic nature acting on species  $\alpha$ . In addition, the electric potential  $\psi$  is given by the solution of eq 7. Unlike the full collision operator of the Enskog type, the last two terms on the right-hand side of eq 13 act only on the hydrodynamic components of the distribution function  $f^{\alpha}$ . The nonhydrodynamic modes instead are driven by the first term on the right-hand side of eq 13, which is a Bhatnagar–Gross–Krook (BGK) type of relaxation kernel. Its role is to drive the system toward local equilibrium over a time scale of  $\omega^{-1}$ , which is much shorter than the hydrodynamic time scales,<sup>34</sup> and the global equilibrium is controlled by the collisional force mentioned above.

The BGK term contains distributions functions  $\phi_{\perp}^{\alpha}$  and  $\phi^{\alpha}$ , which have the following representations (details in ref 35):

$$\phi^{\alpha}(\mathbf{r}, \mathbf{v}, t) = n^{\alpha}(\mathbf{r}, t) \left[ \frac{m^{\alpha}}{2\pi k_{\text{B}}T} \right]^{3/2} \exp\left( -\frac{m^{\alpha}(\mathbf{v} - \mathbf{u}(\mathbf{r}, t))^2}{2k_{\text{B}}T} \right) \quad (14)$$

and

$$\begin{aligned} \phi_{\perp}^{\alpha}(\mathbf{r}, \mathbf{v}, t) = & \phi^{\alpha}(\mathbf{r}, \mathbf{v}, t) \\ & \times \left\{ 1 + \frac{m^{\alpha}(\mathbf{u}^{\alpha}(\mathbf{r}, t) - \mathbf{u}(\mathbf{r}, t)) \cdot (\mathbf{v} - \mathbf{u}(\mathbf{r}, t))}{k_{\text{B}}T} \right\} \end{aligned} \quad (15)$$

Notice that in the case of a one-component fluid there is no difference between  $\phi_{\perp}^{\alpha}$  and  $\phi^{\alpha}$  because the velocities  $\mathbf{u}^{\alpha}$  and  $\mathbf{u}$  coincide and the standard BGK approximation involves the difference between the distribution  $f^{\alpha}$  and the local Maxwellian  $\phi^{\alpha}$ . The above prescription fulfills the indifferenciability principle that states that when all physical properties of the species are identical, the total distribution  $f = \sum_{\alpha} f^{\alpha}$  must obey the single-species transport equation.

The reason to use the modified distributions in eq 15 instead of eq 14 is to obtain the correct mutual diffusion and hydrodynamic properties starting from eq 12. A simple BGK

recipe, that is, by setting  $\phi_{\perp}^{\alpha} = \phi^{\alpha}$ , would lead to double counting the interactions with respect to the diffusive properties.

Equations 12 and 13 can be solved after specifying forces  $\mathbf{F}^{\alpha}$  and  $\Phi^{\alpha}$ , Coulombic force  $-e\sqrt{\nabla\psi(\mathbf{r})}$ , and fluid velocities  $\mathbf{u}$  and  $\mathbf{u}^{\alpha}$ .

From the knowledge of the  $f^{\alpha}$ 's it is possible to determine not only all of the hydrodynamic fields of interest but also the structure of the fluid on the molecular scale. All equations that constitute the building blocks of the classical electrokinetic approach can be derived from eqs 12 and 13. In fact, the PNP and NS equations can be straightforwardly recovered by taking the appropriate velocity moments of the kinetic Enskog–Boltzmann equation. From the distributions, we compute the partial densities  $n^{\alpha}(\mathbf{r}, t)$ ,

$$n^{\alpha}(\mathbf{r}, t) = \int d\mathbf{v} f^{\alpha}(\mathbf{r}, t) \quad (16)$$

the average velocities  $\mathbf{u}^{\alpha}(\mathbf{r}, t)$  of the species  $\alpha$ ,

$$n^{\alpha}(\mathbf{r}, t) \mathbf{u}^{\alpha}(\mathbf{r}, t) = \int d\mathbf{v} \mathbf{v} f^{\alpha}(\mathbf{r}, t) \quad (17)$$

and the kinetic contribution of component  $\alpha$  to the pressure tensor,

$$\pi_{ij}^{\alpha}(\mathbf{r}, t) = m^{\alpha} \int d\mathbf{v} (v_i - u_i)(v_j - u_j) f^{\alpha}(\mathbf{r}, \mathbf{v}, t) \quad (18)$$

The explicit form of the internal forces  $\Phi^{\alpha}(\mathbf{r}, t)$  featured in eq 13 is determined by taking the first moment of the collision integral with respect to the velocity. By algebraic manipulations, one observes that  $\Phi^{\alpha}(\mathbf{r}, t)$  is due to two-particle correlations and can be separated into three contributions,<sup>31</sup> as

$$\Phi^{\alpha}(\mathbf{r}, t) = \mathbf{F}^{\alpha, \text{mf}}(\mathbf{r}, t) + \mathbf{F}^{\alpha, \text{drag}}(\mathbf{r}, t) + \mathbf{F}^{\alpha, \text{visc}}(\mathbf{r}, t) \quad (19)$$

The first term arises from the gradient of the hard sphere chemical potential excess over the ideal gas value

$$\mathbf{F}^{\alpha, \text{mf}}(\mathbf{r}, t) = -\nabla \mu_{\text{exc}}^{\alpha}(\mathbf{r}, t) \quad (20)$$

with

$$\nabla \mu_{\text{exc}}^{\alpha} = k_{\text{B}}T \sum_{\beta} (\sigma^{\alpha\beta})^2 \int d\hat{\mathbf{s}} \hat{\mathbf{s}} g_{\alpha\beta}(\mathbf{r}, \mathbf{r} + \sigma^{\alpha\beta} \hat{\mathbf{s}}, t) n_{\beta}(\mathbf{r} + \sigma^{\alpha\beta} \hat{\mathbf{s}}, t) \quad (21)$$

where the integration is over the surface of the unit sphere and  $g^{\alpha\beta}(\mathbf{r}, \mathbf{r} + \sigma^{\alpha\beta} \hat{\mathbf{s}}, t)$  is the inhomogeneous pair correlation functions for hard spheres at contact ( $|\mathbf{r} - \mathbf{r}'| = \sigma^{\alpha\beta}$ ). The second term accounts for the frictional force between the ions and the solvent and depends linearly on their relative velocities

$$\mathbf{F}^{\alpha, \text{drag}}(\mathbf{r}, t) = -\sum_{\beta} \gamma^{\alpha\beta}(\mathbf{r}, t) (\mathbf{u}^{\alpha}(\mathbf{r}, t) - \mathbf{u}^{\beta}(\mathbf{r}, t)) \quad (22)$$

via the inhomogeneous friction tensor

$$\begin{aligned} \gamma_{ij}^{\alpha\beta}(\mathbf{r}, t) = & 2(\sigma^{\alpha\beta})^2 \sqrt{\frac{2\mu^{\alpha\beta} k_{\text{B}}T}{\pi}} \\ & \times \int d\hat{\mathbf{s}} s_i s_j g^{\alpha\beta}(\mathbf{r}, \mathbf{r} + \sigma^{\alpha\beta} \hat{\mathbf{s}}, t) n^{\beta}(\mathbf{r} + \sigma^{\alpha\beta} \hat{\mathbf{s}}, t) \end{aligned} \quad (23)$$

where  $\mu^{\alpha\beta}$  is the reduced mass  $\mu^{\alpha\beta} = (m^{\alpha} m^{\beta}) / (m^{\alpha} + m^{\beta})$  for the colliding pair. Notice the local character of the relation between the drag force and the fluid velocity. Finally, the particles experience a viscous force that has the following

Enskog form:

$$\begin{aligned} \mathbf{F}^{\alpha, \text{visc}}(\mathbf{r}, t) &= \sum_{\beta} 2(\sigma^{\alpha\beta})^2 \sqrt{\frac{2\mu^{\alpha\beta} k_B T}{\pi}} \\ &\times \int d\hat{\mathbf{s}} \hat{\mathbf{s}} g_{\alpha\beta}(\mathbf{r}, \mathbf{r} + \sigma^{\alpha\beta} \hat{\mathbf{s}}, t) n^{\beta}(\mathbf{r} + \sigma^{\alpha\beta} \hat{\mathbf{s}}, t) \hat{\mathbf{s}} \cdot \\ &(\mathbf{u}^{\beta}(\mathbf{r} + \sigma^{\alpha\beta} \hat{\mathbf{s}}) - \mathbf{u}^{\beta}(\mathbf{r})) \end{aligned} \quad (24)$$

Because there is no exact theory of the pair correlation function in spatially inhomogeneous systems, the contact value of  $g^{\alpha\beta}$  is computed using a two-component generalization of the Fischer and Methfessel prescription:<sup>37</sup> one approximates the inhomogeneous  $g^{\alpha\beta}$  by the corresponding bulk value evaluated when the partial densities take the values of the smeared densities,  $\bar{n}^{\alpha}(\mathbf{r})$

$$g^{\alpha\beta}(\mathbf{r}_{\omega}, \mathbf{r}_{\beta}; |\mathbf{r}^{\alpha} - \mathbf{r}^{\beta}| = \sigma^{\alpha\beta}) = g_{\text{bulk}}^{\alpha\beta}(\{\bar{\xi}_n(\mathbf{R}^{\alpha\beta})\}) \quad (25)$$

where the function

$$\bar{\xi}_n(\mathbf{R}^{\alpha\beta}) = \frac{\pi}{6} \sum_{\alpha} \bar{n}^{\alpha}(\mathbf{R}^{\alpha\beta}) (\sigma^{\alpha\alpha})^n$$

is a linear combinations of the smeared densities

$$\bar{n}^{\alpha}(\mathbf{R}^{\alpha\beta}) = \frac{1}{V^{\alpha}} \int_{V^{\alpha}} d\mathbf{r} n^{\alpha}(\mathbf{r} - \mathbf{R}^{\alpha\beta})$$

over spheres of volume  $V^{\alpha} = \pi(\sigma^{\alpha\alpha})^3/6$  centered at the point  $\mathbf{R}^{\alpha\beta} = (\mathbf{r}^{\alpha} + \mathbf{r}^{\beta})/2$ , where  $\mathbf{r}^{\alpha}$  and  $\mathbf{r}^{\beta}$  are the centers of the two spheres. The explicit expression for  $g_{\text{bulk}}^{\alpha\beta}$  is provided by an extension of the Carnahan–Starling equation to mixtures:<sup>38,39</sup>

$$\begin{aligned} g_{\text{bulk}}^{\alpha\beta}(\{\xi_n\}) &= \frac{1}{1 - \xi_3} + \frac{3}{2} \frac{\sigma^{\alpha\alpha} \sigma^{\beta\beta}}{\sigma^{\alpha\beta}} \frac{\xi_2}{(1 - \xi_3)^2} \\ &+ \frac{1}{2} \left( \frac{\sigma^{\alpha\alpha} \sigma^{\beta\beta}}{\sigma^{\alpha\beta}} \right)^2 \frac{\xi_2^2}{(1 - \xi_3)^3} \end{aligned} \quad (26)$$

We remark that the present method requires a knowledge of the pair correlation function at contact, in contrast with the DDFT approach that requires instead a knowledge of the free energy or equivalently the Ornstein–Zernike direct correlation function. However, in the spirit of the method here employed, it is equivalent to the so-called weighted density approximation of equilibrium DFT. The latter does not contain information necessary to compute the transport coefficients, which in the present method are obtained from  $g^{\alpha\beta}$  via the Enskog ansatz for the collision integrals.

**3.1. Derivation of the Electrokinetic Equations from the Microscopic Approach.** It is useful to show that in the limit of slowly varying fields the transport equations (eq 12) reproduce the macroscopic evolution discussed in Section 2.1. For this purpose, we integrate eq 12 with respect to the velocity and obtain the conservation law for the number of particles of each species:

$$\begin{aligned} \frac{\partial}{\partial t} n^{\alpha}(\mathbf{r}, t) &= -\nabla \cdot (n^{\alpha}(\mathbf{r}, t) (\mathbf{u}^{\alpha}(\mathbf{r}, t) - \mathbf{u}(\mathbf{r}, t))) \\ &- \nabla \cdot (n^{\alpha}(\mathbf{r}, t) \mathbf{u}(\mathbf{r}, t)) \\ &= -\nabla \cdot \mathbf{J}^{\alpha}(\mathbf{r}, t) \end{aligned} \quad (27)$$

To recover the PNP equation, we consider the momentum balance equation for species  $\alpha$ , which is obtained after multiplying by  $\mathbf{v}$  and integrating with respect to  $\mathbf{v}$ :

$$\begin{aligned} \frac{\partial}{\partial t} [n^{\alpha}(\mathbf{r}, t) u_j^{\alpha}(\mathbf{r}, t)] &+ \nabla_i (n^{\alpha}(\mathbf{r}, t) u_i^{\alpha}(\mathbf{r}, t) u_j^{\alpha}(\mathbf{r}, t)) \\ &- n^{\alpha}(\mathbf{r}, t) (u_i^{\alpha}(\mathbf{r}, t) - u_i(\mathbf{r}, t)) (u_j^{\alpha}(\mathbf{r}, t) - u_j(\mathbf{r}, t)) \\ &= -\nabla_i \frac{\pi_{ij}^{\alpha}(\mathbf{r}, t)}{m^{\alpha}} + \frac{F_j^{\alpha}(\mathbf{r})}{m^{\alpha}} n^{\alpha}(\mathbf{r}, t) + \frac{\Phi_j^{\alpha}(\mathbf{r}, t)}{m^{\alpha}} n^{\alpha}(\mathbf{r}, t) \\ &- \frac{ez^{\alpha}}{m^{\alpha}} n^{\alpha}(\mathbf{r}, t) \nabla_j \psi(\mathbf{r}, t) \end{aligned} \quad (28)$$

Using eq 20, we define the gradient of the global chemical potential of the individual species,  $\mu^{\alpha}$ , as the sum of the ideal gas part and the excess part:

$$n^{\alpha}(\mathbf{r}, t) \nabla_i \mu^{\alpha}(\mathbf{r}, t) = \nabla_j \pi_{ij}^{\alpha}(\mathbf{r}, t) \delta_{ij} - n^{\alpha}(\mathbf{r}, t) F_i^{\alpha, \text{mf}}(\mathbf{r}, t) \quad (29)$$

By assuming the existence of a steady current, we drop the nonlinear terms in the velocities on the left-hand side of eq 28 and neglect the viscous force contribution. The following approximated force balance is obtained:

$$\Delta \mu^{\pm}(\mathbf{r}, t) - \mathbf{F}^{\pm}(\mathbf{r}) + ez^{\pm} \nabla \psi(\mathbf{r}, t) \approx \mathbf{F}^{\pm, \text{drag}}(\mathbf{r}, t) \quad (30)$$

The right-hand side of eq 30 represents the drag force exerted on particles of type  $\alpha = \pm$ , by reason of their different drift velocities. In dilute solutions, the charged components are expected to experience a large friction arising only from the solvent but a negligible friction from the oppositely charged species so that we further approximate

$$\mathbf{F}^{\pm, \text{drag}}(\mathbf{r}, t) = -\gamma^{\pm}(\mathbf{r}, t) (\mathbf{u}^{\pm}(\mathbf{r}, t) - \mathbf{u}(\mathbf{r}, t)) \quad (31)$$

where we set  $\mathbf{u} \approx \mathbf{u}^0$ . In eq 31, the friction can be evaluated under uniform bulk conditions to be

$$\gamma^{\pm} \approx \frac{8}{3} \sqrt{2\pi k_B T \frac{m^{\pm} m^0}{m^{\pm} + m^0}} g^{0\pm} n^0 (\sigma^{0\pm})^2 \quad (32)$$

with  $n^0$  being the bulk density of the solvent and  $g_{0\pm}$  being the bulk ion–solvent pair correlation function evaluated at contact. Finally, using eqs 27 and 31 we obtain an expression for the ionic currents in terms of the microscopic parameters

$$\begin{aligned} \mathbf{J}_i^{\pm}(\mathbf{r}, t) &= -\frac{1}{\gamma^{\pm}} n^{\pm}(\mathbf{r}, t) \nabla \mu^{\pm}(\mathbf{r}, t) \\ &- \frac{1}{\gamma^{\pm}} ez^{\pm} n^{\pm}(\mathbf{r}, t) \nabla \psi(\mathbf{r}, t) + n^{\pm}(\mathbf{r}, t) \mathbf{u}(\mathbf{r}, t) \end{aligned} \quad (33)$$

which has the same form as the phenomenological Planck–Nernst current eq 6, with the full chemical potential gradient  $\mu^{\pm}$  replacing the ideal gas chemical potential gradient:  $k_B T \nabla \ln(n^{\alpha})$ ,  $\gamma^{\pm} = k_B T/D^{\pm}$ , and  $\lambda^{\pm} = 1/\gamma^{\pm}$ . The total electric charge density current is

$$\mathbf{J}_e = -\sum_{\pm} \frac{ez^{\pm}}{\gamma^{\pm}} n^{\pm}(\mathbf{r}, t) \nabla \mu^{\pm}(\mathbf{r}, t) + \sigma_{\text{el}} \mathbf{E} + \rho_e(\mathbf{r}, t) \mathbf{u}(\mathbf{r}, t) \quad (34)$$

where the zero-frequency electric conductivity  $\sigma_{\text{el}}$  is given by the Drude–Lorentz-like equation

$$\sigma_{\text{el}} = e^2 \left( \frac{(z^+)^2}{\gamma^+} n^+(\mathbf{r}, t) + \frac{(z^-)^2}{\gamma^-} n^-(\mathbf{r}, t) \right) \quad (35)$$

showing that the conductivity is due to collisions with the solvent and decreases as the solvent becomes denser ( $\gamma^{\pm}$  is an increasing function of  $n^0$ ) but increases with the number of charge carriers. It should be noticed that, in the approximation of a local friction, the

Drude–Lorentz conductivity is local in space and time. However, in the numerical solution this local approximation is not imposed.

To derive the total momentum equation, already introduced on a phenomenological basis in eq 9, we sum eq 28 over the three components

$$\begin{aligned} \partial_t u_j(\mathbf{r}, t) + u_i(\mathbf{r}, t) \nabla_i u_j(\mathbf{r}, t) + \frac{1}{\rho_m} \nabla_i \pi_{ij}^{(K)} \\ + \frac{1}{\rho_m} \sum_{\pm} e z^{\pm} n^{\pm}(\mathbf{r}, t) \nabla_j \psi(\mathbf{r}, t) \\ - \frac{1}{\rho_m} \sum_{\alpha=0,\pm} n^{\alpha}(\mathbf{r}, t) (F_j^{\alpha}(\mathbf{r}) + F_j^{\alpha, mf}(\mathbf{r}, t) \\ + F_j^{\alpha, visc}(\mathbf{r}, t)) = 0 \end{aligned} \quad (36)$$

where  $\pi_{ij}^{(K)}(\mathbf{r}, t) = \sum_{\alpha} \pi_{ij}^{\alpha}(\mathbf{r}, t)$  is the total kinetic pressure that can be approximated as

$$\nabla_i \pi_{ij}^{(K)} \simeq \delta_{ij} \nabla_j P_{id} - \eta^{(K)} \left( \frac{1}{3} \nabla_i \nabla_j u_i + \nabla_i^2 u_j \right) \quad (37)$$

with  $P_{id} = k_B T \sum_{\alpha} n^{\alpha}$  and  $\eta^{(K)} = (k_B T / \omega) \sum_{\alpha} n^{\alpha}$ . Using the results in ref 31, we can write

$$\begin{aligned} \sum_{\alpha} n^{\alpha}(\mathbf{r}, t) \mathbf{F}^{\alpha, visc}(\mathbf{r}, t) \\ \simeq -\eta^{(C)} \nabla^2 \mathbf{u} - \left( \frac{1}{3} \eta^{(C)} + \eta_b^{(C)} \right) \nabla (\nabla \cdot \mathbf{u}) \end{aligned} \quad (38)$$

The nonideal contribution to the shear viscosity is evaluated under uniform bulk conditions to be

$$\eta^{(C)} = \frac{4}{15} \sum_{\alpha\beta} \sqrt{2\pi\mu^{\alpha\beta} k_B T} (\sigma^{\alpha\beta})^4 g^{\alpha\beta} n_0^{\alpha} n_0^{\beta} \quad (39)$$

whereas the bulk viscosity is  $\eta_b^{(C)} = (5/3)\eta^{(C)}$ . In conclusion, eq 36 can be cast in the Navier–Stokes form

$$\begin{aligned} \partial_t u_j + u_i \nabla_i u_j = -\frac{1}{\rho_m} \nabla_i P \delta_{ij} - \frac{\rho_e}{\rho_m} \nabla_j \psi + \frac{\eta}{\rho_m} \nabla_i \nabla_j u_i \\ + \frac{\frac{1}{3}\eta + \eta_b}{\rho_m} \nabla_j \nabla_i u_i \end{aligned} \quad (40)$$

with  $\eta = \eta^{(K)} + \eta^{(C)}$  and  $\nabla_i P = \nabla_i P_{id} + \sum_{\alpha} n^{\alpha}(\mathbf{r}, t) \nabla_i \mu_{exc}^{\alpha}(\mathbf{r}, t)$ .

Having established the correspondence between the macroscopic equations and those derived from the kinetic approach, we can now outline the method of solution.

**3.2. Entropic Contribution to the Poisson–Boltzmann Equation in the Nonprimitive Model.** Some recent studies on the nonprimitive model of ionic solution lead to a modified Poisson–Boltzmann equation.<sup>40,42</sup> In the same spirit, we derive within the present approach a similar equation. We consider only mixtures of equal sizes. At equilibrium, that is, when all of the currents vanish, according to eq 33 the ionic densities satisfy the equations

$$k_B T \nabla \ln n^{\pm}(\mathbf{r}, t) + \nabla \mu_{exc}^{\pm}(\mathbf{r}, t) + e z^{\pm} \nabla \psi(\mathbf{r}) = 0 \quad (41)$$

and the solvent satisfies the equation

$$k_B T \nabla \ln n^0(\mathbf{r}, t) + \nabla \mu_{exc}^0(\mathbf{r}, t) = 0 \quad (42)$$

Notice that because for equally sized molecules  $\mu^{exc}$  depends only on the overall local packing fraction, one can write

$$k_B T (\nabla \ln(n^{\pm}(\mathbf{r}, t) - \nabla \ln(n^0(\mathbf{r}, t)) + e z^{\pm} \nabla \psi(\mathbf{r})) = 0 \quad (43)$$

and by integrating one gets an expression relating the ionic densities to the solvent density

$$n^{\pm}(\mathbf{r}, t) = C^{\pm} n^0(\mathbf{r}, t) \exp\left(-\frac{e z^{\pm} \psi(\mathbf{r})}{k_B T}\right) \quad (44)$$

where  $C^{\pm}$  is an integration constant to be found by normalization.

As a result, the electrostatic potential is coupled to the solvent density via the Poisson equation:

$$\nabla^2 \psi(\mathbf{r}, t) = -\frac{e}{\epsilon} n^0(\mathbf{r}, t) \sum_{\pm} z^{\pm} C^{\pm} \exp\left(-\frac{e \sum_{\pm} z^{\pm} \psi(\mathbf{r}, t)}{k_B T}\right) \quad (45)$$

In the case of the restricted primitive model (no explicit solvent), the density of the “ghost” solvent is reabsorbed in the definition of the integration constant. The numerical test of such a relation is given below in Section 5.

#### 4. NUMERICAL METHOD

The numerical solution of the coupled equations for the distribution functions  $f^{\alpha}$ , (eq 12) is achieved in the framework of the lattice Boltzmann method, as presented in refs 31 and 35. The numerical method is a substantial modification of the conventional method used in fluid dynamics applications with respect to the presence of hard sphere collisions.<sup>28</sup> In a nutshell, the lattice Boltzmann method is based on the following steps. One discretizes the position coordinate,  $\mathbf{r}$ , by introducing a Cartesian mesh whose lattice points are separated by a distance  $a$ . The continuous velocity,  $\mathbf{v}$ , is also discretized by restricting its values to  $Q$  possible states,  $\mathbf{v} \rightarrow \{\mathbf{c}_p\}$  with  $p = 1, N$ . The discrete velocities are chosen so as to connect neighboring spatial mesh points. For the present 3D study, we use a 19-speed lattice consisting of 1 speed  $\mathbf{c}_p = 0$  (particle at rest on a mesh node), 6 discrete velocities with  $|\mathbf{c}_p| = 1$  and pointing toward the first mesh neighbors, and 12 particles with  $|\mathbf{c}_p| = 2^{1/2}$  pointing toward the second mesh neighbors. The continuous phase space distribution functions  $f^{\alpha}$  are replaced by the array  $f^{\alpha}(\mathbf{r}, \mathbf{v}, t) \rightarrow f_p^{\alpha}(\mathbf{r}, t)$ , and the velocity moments are evaluated as<sup>28</sup>

$$n^{\alpha}(\mathbf{r}, t) = \sum_p f_p^{\alpha} \quad (46)$$

and

$$n^{\alpha}(\mathbf{r}, t) \mathbf{u}^{\alpha}(\mathbf{r}, t) = \sum_p \mathbf{c}_p f_p^{\alpha}(\mathbf{r}, t) \quad (47)$$

The modification of the conventional Lattice Boltzmann method to the case of hard sphere dynamics is based on computing the forces encoded by eqs 21, 24, and 31 via numerical quadratures. The presence of Coulomb forces requires the solution of the Poisson equation for the electrostatic potential generated by the mobile and surface charges. Its determination is achieved by using a successive over-relaxation method.<sup>14</sup> The speed of convergence of the Poisson solver is greatly enhanced by employing a Gauss–Siedel checkerboard scheme in conjunction with Chebychev acceleration.<sup>14</sup> Neumann boundary conditions on the gradient of the electrostatic potential are imposed at the wall surface

$$\hat{n} \cdot \nabla \psi|_{\mathbf{r} \in S} = -\frac{\Sigma(\mathbf{r})}{\epsilon} \quad (48)$$

where  $\hat{n}$  is the normal to the surface,  $S$ . We impose an external voltage by emulating the presence of electrodes in real systems. The method implies imposing the value of the external electric field  $E_x$  as the boundary condition

$$\nabla\psi = -E_x \quad (49)$$

at locations  $x = 0^+$  and  $x = L^-$ .

The electrostatic boundary conditions are imposed by using a second-order finite difference scheme compatible with the overall accuracy of the lattice Boltzmann method. The system is further taken to be periodic along the  $x$  direction for the fluid populations of each component. This choice implies that all hydrodynamic fields (density, currents, etc.) are periodic along the  $x$  direction. To accommodate the presence of the electrodes, the hydrodynamic fields exhibit a finite jump at the  $x = 0, L, 2L, \dots$  locations. Preliminary calculations have shown that this jump does not have a major impact on the stationary quantities, in particular, with regard to those in the pore region. No slip boundary conditions on the fluid velocities of each species are imposed by means of the bounce-back rule.<sup>28</sup> Once all forces on the right-hand side of eq 12 are computed, we evolve the distribution function by a second-order accurate trapezoidal integration.<sup>36</sup> In addition, we compensate for the harsh internal forces by properly chosen auxiliary fields. This method improves the accuracy and robustness of the numerical scheme without altering the structure and dynamics of the system. Full details can be found in ref 36.

## 5. RESULTS

We have conducted numerical experiments on channels of three different shapes, as illustrated in Figure 1. Such a choice is intended to capture the behavior of a large class of solid-state devices and biological ionic channels (i.e., macromolecular pores that control the passage of ions across cell membranes). As shown in Figure 1, in system A the fluid mixture is confined to move between two uniformly charged parallel plates. Such a geometry is useful in studying the electroosmotic flow and ionic current when the plate separation  $H$  is on the order of the Debye length.<sup>7</sup> In system B, the surface charge of the areal density  $\Sigma$  covers only two rectangular regions of area  $\mathcal{A}$  and longitudinal size  $a$  on opposite walls. Finally, system C is obtained by considering a parallel slit containing a narrowing of length  $L$ . Such a striction forms an open wedge, where the planes are separated by a distance  $h$  at the small opening and  $H$  at the large opening. The wedge geometry recalls the shape of synthetic conical nanopores, which have been manufactured and studied in recent years<sup>44–46</sup> in order to understand the origin of rectifying devices, as related to biological channels.

It is important to remark that, for models B and C, away from the charged region we do not explicitly model a completely macroscopic reservoir. Rather, the far-away region acts as a buffer that allows us to recover electroneutrality sufficiently far away from the charged region, as detailed in the following text. Given the studied geometries, it is of little use to compute characteristic curves and compare them directly with the experimental data obtained in electrolytic cells, as studied by Siwy and co-workers,<sup>44,45</sup> whereas our systems are more alike series of nanodevices.

Throughout this article we shall use lattice units defined in the following. Time is measured in units of the discrete step  $\Delta t = 1$ , lengths are measured in units of lattice spacing, and the charge  $e$  and mass  $m$  are assumed to be unitary. The thermal energy  $k_B T$  is specified by fixing the thermal velocity whose value is

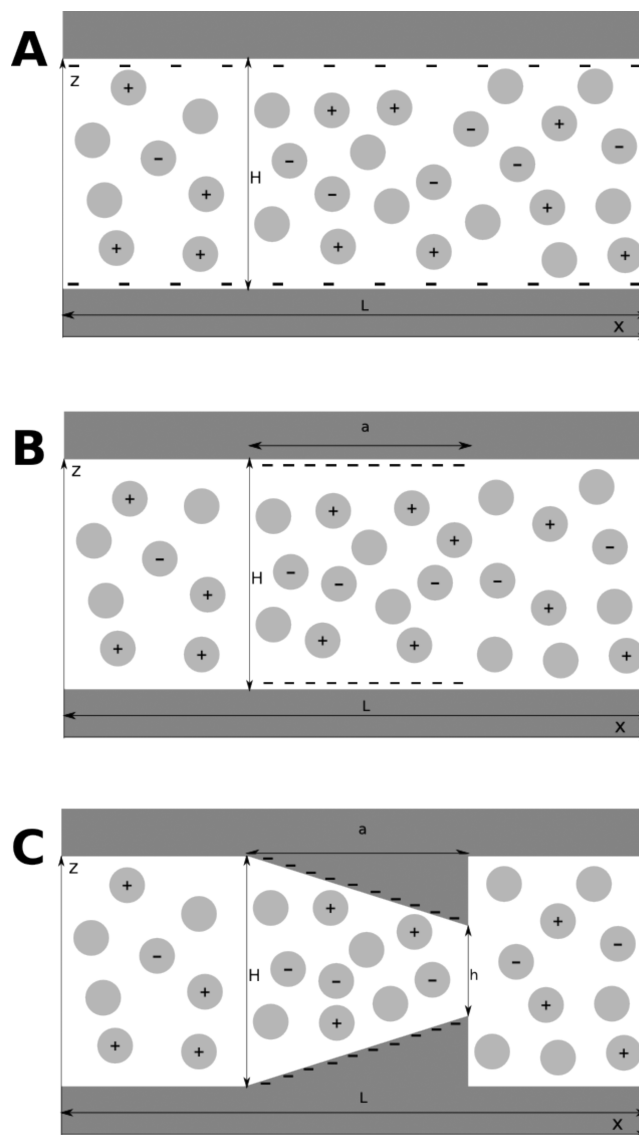


**Figure 1.** Geometries of model systems A–C, with the shaded regions representing the wall. Each system contains three species of hard spheres of equal diameters  $\sigma$  and masses  $m$  but different charges: 0, 1, and  $-1$ , respectively. In model A, the ternary fluid moves in a channel whose walls are uniformly and negatively charged. The system is globally neutral:  $N^+ - N^- = -2\Sigma wL/e$  where  $N^+$  and  $N^-$  are the numbers of positive and negative mobile charges, respectively,  $\Sigma$  is the surface charge density, and  $w$  is the transversal dimension of the channel and  $L$  is its length. Model B mimics a parallel slit channel whose walls are decorated with negative surface charge density  $\Sigma$  in a region of length  $a$ . Charge neutrality,  $N^+ - N^- = -2\Sigma wa/e$ , holds. In model C, a wedge-shaped region of length  $a$  connects two parallel slits. The surface charge sits only on the inclined walls and  $N^+ - N^- = -2\Sigma w(a^2 + (H - h)^2/4)^{1/2}/e$ . In our simulations, the sizes of the large and small openings,  $H$  and  $h$ , are kept fixed.

$v_T = (k_B T/m)^{1/2} = 1/3^{1/2}$  in lattice units. The dielectric constant is obtained by fixing the Bjerrum length,  $l_B = e^2/(4\pi\epsilon k_B T)$ , which is the distance at which the thermal energy  $k_B T$  is equal to the electrostatic energy between two unit charges. We remind the reader that in water under ambient conditions and for two monovalent ions this length is  $l_B \approx 0.7$  nm; therefore, we set  $l_B/\sigma = 4$ .

We consider mixtures of hard spheres of equally sized diameter  $\sigma^{\alpha\alpha} \equiv \sigma = 4$  in lattice units. The packing fraction is fixed

to  $(\pi/6)\sum_{\alpha} n^{\alpha}(\sigma^{\alpha\alpha})^3 = 0.20$ . The surface charge density  $\Sigma$  is always taken to be negative and has a typical value of  $\Sigma\sigma^2/e = 10^{-3}$ . At the initial time, the densities of the ions in the channel are set by fixing the Debye length in the bulk

$$\lambda_D = \sqrt{\frac{\epsilon k_B T}{2e^2 n_s}} = \sqrt{\frac{1}{8\pi l_B n_s}} \quad (50)$$

where  $n_s$  is the average density of a single ionic species in the bulk. This relation is used to define the initial density of the minority ions (the co-ions) to  $n^-(\mathbf{r}) = n_s$ . Next, we impose a global electroneutrality condition in order to set the local density of counterions as

$$e \int_V (n^+(\mathbf{r}) - n^-(\mathbf{r})) d\mathbf{r} + \int_S \Sigma(\mathbf{r}) d\mathbf{r} = 0 \quad (51)$$

where the first integral extends over the volume of the system and the second extends over its surface. During the simulation, the number of particles of each species is fixed, and as time marches on, the densities rearrange according to their intrinsic evolutions. We fix the value at the Debye length to  $\lambda_D/\sigma = 2.75$ , unless differently stated.

To fix the physical units by stipulating that  $\sigma = 3 \times 10^{-10}$  m, we consider a mixture with number densities  $n^0\sigma^3 = 0.392$  and  $n^{\pm}\sigma^3 = 0.001408$ , corresponding to a 0.1 M solution. The friction coefficient  $\gamma$  for such mixture is about 0.5, and the electric conductivity is  $\sigma_{el} = 8 \times 10^{-5}$ . Finally, the geometrical parameters of the pore are set to  $H/\sigma = 12.5$ ,  $h/\sigma = 2.75$ , and  $a/\sigma = 10$ .

In the following text, we compare the results at the finite packing fraction with the results obtained in the absence of HS collisions, that is, at a negligible packing fraction. The former is useful for singling out the role of molecular interactions, and the latter corresponds to the simple Bhatnagar–Gross–Krook approximation, that is, the completely macroscopic picture.

Although the numerical method produces complete time-dependent solutions, we focus on studying stationary conditions for the sake of simplicity. For each simulated system, the convergence toward stationarity is fast ( $\sim 2000$  iterations) and in general very stable. In the near future, we plan to explore time-dependent phenomena, as under alternate electric field conditions.

As a preliminary test, we validate the equilibrium properties of the system because in the absence of ionic currents the theory predicts a simple local relation between the species densities and the electric potential obtained as an immediate consequence of eq 44

$$\frac{n^+(\mathbf{r}, t)}{n^-(\mathbf{r}, t)} = \frac{C^+}{C^-} \exp\left(-\frac{2ez^{\pm}\psi(\mathbf{r})}{k_B T}\right) \quad (52)$$

and

$$\frac{n^+(\mathbf{r}, t) n^-(\mathbf{r}, t)}{n_0^2(\mathbf{r}, t)} = C^+ C^- \quad (53)$$

That is, the ratio of the density profile probes the electrostatic field  $\psi(\mathbf{r}, t)$  whereas the product of the two profiles should be everywhere proportional to the square of the density of the solvent. These ratios are displayed in Figures 2 and 3, and the agreement is quite good for both tests. Joly and co-workers have performed a similar test in their study,<sup>40</sup> but in contrast to our method, they made the comparison by utilizing the density profiles obtained from the MD simulation of a ternary charged mixture. In the present calculation, instead both the electric potential and the density profiles are obtained from the same numerical calculation in a self-consistent fashion.

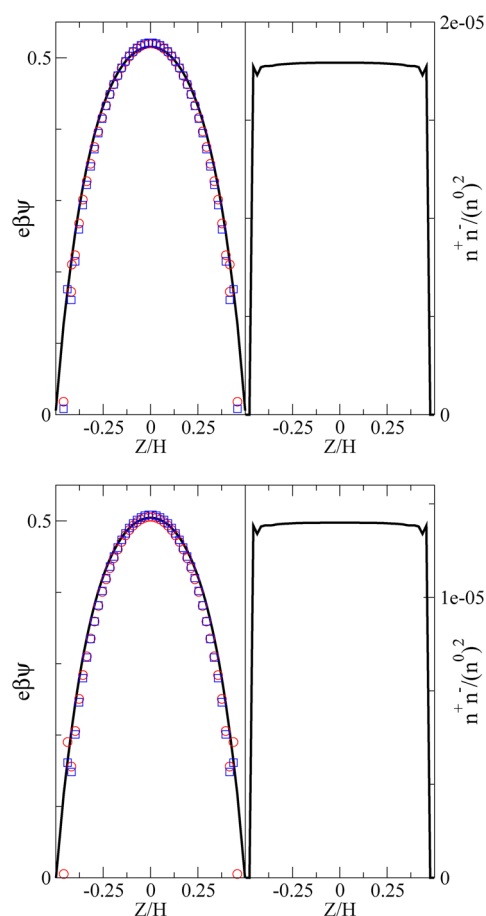


**Figure 2.** Validation of the equilibrium conditions (eqs 52 and 53) for models A (upper panel) and B (lower panel). The left panels report the transversal profiles of the scaled potential  $e\psi/k_B T$  (solid curves) and  $A + \ln(n^0/n^+)$  (circles) and  $B - \ln(n^0/n^-)$  (squares), with  $A$  and  $B$  being constants. The right panels report the transversal profile of the product  $n^+ n^- / (n^0)^2$ . All profiles are taken at  $x = L/2$ .

The use of the full Poisson equation in connection with a hard sphere fluid disregards the effect of charge correlations.<sup>41</sup> This effect has been included by some authors<sup>11</sup> using the mean spherical approximation (MSA) representation of the direct pair correlation function. At the MSA level, the exclusion region of hard spheres is removed from the source term of eq 7. We have thus considered this correction to the electrostatic forces by removing the contribution

$$\begin{aligned} & -\frac{1}{\epsilon} \int_{|\mathbf{r}-\mathbf{r}'|<\sigma} d\mathbf{r}' \rho_e(\mathbf{r}') \frac{(\mathbf{r}'-\mathbf{r})}{|\mathbf{r}-\mathbf{r}'|^3} \\ & = -\frac{1}{\epsilon} \int_{|\mathbf{r}-\mathbf{r}'|<\sigma} d\mathbf{r}' (\rho_e(\mathbf{r}') - \rho_e(\mathbf{r})) \frac{(\mathbf{r}'-\mathbf{r})}{|\mathbf{r}-\mathbf{r}'|^3} \end{aligned} \quad (54)$$

from the interaction. Notice that the second part of eq 54 is a simple rewriting of the left-hand side that regularizes the integral and avoids numerical overflows. The profiles of the counterions with and without the correction (eq 54) are reported in Figure 4. It is apparent that at the molarities of interest as used in the present work the effect of interactions arising from inner cores is very small for large and narrow pores and can be safely ignored in the simulations.

A further test of the quality of the theoretical framework comes from comparing the equilibrium density profiles with the results of MD simulations of a ternary mixture confined between two

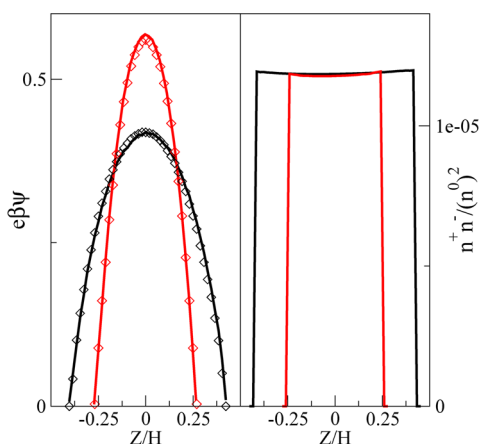


**Figure 3.** Same as Figure 2 for model C. The left panels report the transversal profiles of scaled potential  $e\psi/k_B T$  (solid curves) and  $A + \ln(n^0/n^+)$  (diamonds), with  $A$  being a constant. The right panels report the transversal profile of the product  $n^+ n^- / (n^0)^2$ . The curves are transversal profiles taken at the larger pore mouth (black line and symbols) and at the midpoint of the channel (red line and symbols).

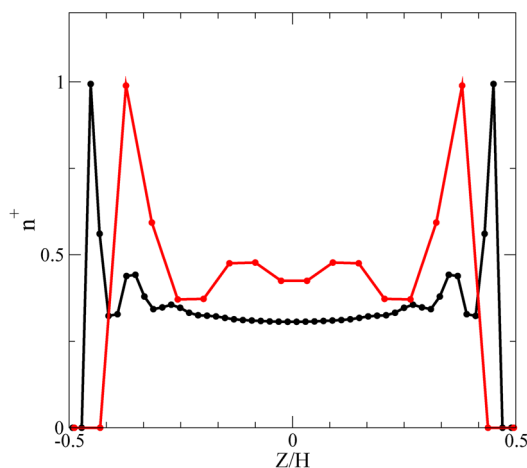


**Figure 4.** (Model A) Density profile of the counterions obtained with the full electrostatic interactions (eq 7) and subtracted by the contribution of eq 54 for packing fraction 0.20,  $\Sigma = -0.0003$ , and for channel widths  $H/\sigma = 12.5$  (black line and red symbols) and  $H/\sigma = 4.5$  (red line and red symbols). The profiles have been rescaled by their maximum value for the sake of readability and are virtually indistinguishable.

parallel slabs of opposite surface charge, that is, a slight variation of model A. In the MD simulations, the excluded volume interactions are modeled via a Lennard-Jones potential

$$V_{LJ}(r_{ij}) = 4\epsilon \left[ \left( \frac{\sigma}{r_{ij}} \right)^{12} - \left( \frac{\sigma}{r_{ij}} \right)^6 \right] \quad (55)$$

truncated at the cutoff so that  $V_{LJ} = 0$  for  $r_{ij} > 2^{1/6}\sigma$ . The particles are repelled from the slab walls by the same type of interaction. In addition, the electrostatic forces are computed via the Ewald summation method for a periodic system.<sup>43</sup> The MD simulations are performed at constant volume and temperature, with parameters of  $\epsilon/k_B T = 2.5$  and  $\sigma = 2$ . The comparison between the electrokinetic and MD results is done by determining the exclusion radius of the soft spheres used in MD, that is, by finding the effective distance  $r^*$  such that  $V_{LJ}(r^*) = k_B T$ . An analogous

procedure is applied to determine the effective volume of the confining slab and, in this way, to match the densities of each component between the electrokinetic and MD simulations. The MD profiles are accumulated over  $10^7$  time steps and for two different slabs of width  $H/\sigma = 10$  and  $4.5$ , filled with  $\sim 2000$  and  $\sim 4000$  particles resulting in packing fractions of 0.10 and 0.20, respectively. To accumulate sufficient statistics, we perform the MD simulations at sufficiently high molarities corresponding to a density of  $n^\pm = 2.0 \times 10^{-5}$ . The electrokinetic and MD profiles reported in Figure 5 are in excellent agreement, in particular, for

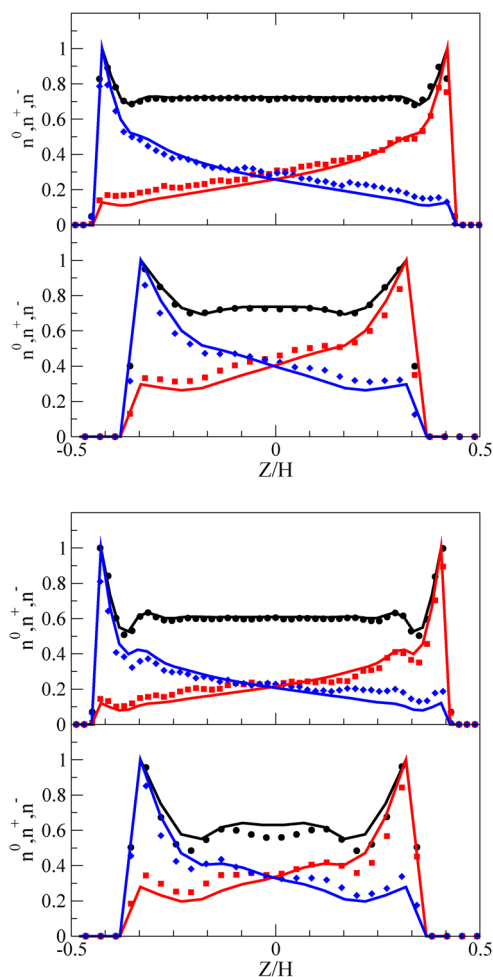


**Figure 5.** Comparison of density profiles as obtained from the electrokinetic method and MD simulations for an equivalent soft sphere system. Simulation details are reported in the text. All profiles have been rescaled by their maximum value for the sake of readability.

the larger slab width. The quality of the results does not seem to deteriorate with the packing fraction considered here. The above results are particularly reassuring in view of the small molarity accessible by the electrokinetic methodology and overall provides good confidence with respect to the simulation framework.

One of the reasons for studying wedged channels having a nanometric orifice is the current rectification properties of this type of device. In the past, such behavior has been ascribed to a ratchet mechanism arising from the joint effect of the asymmetric electrostatic potential within the pore region and departures from thermal equilibrium.<sup>44,45</sup> Alternatively, it has been proposed that rectification arises from the inhomogeneous

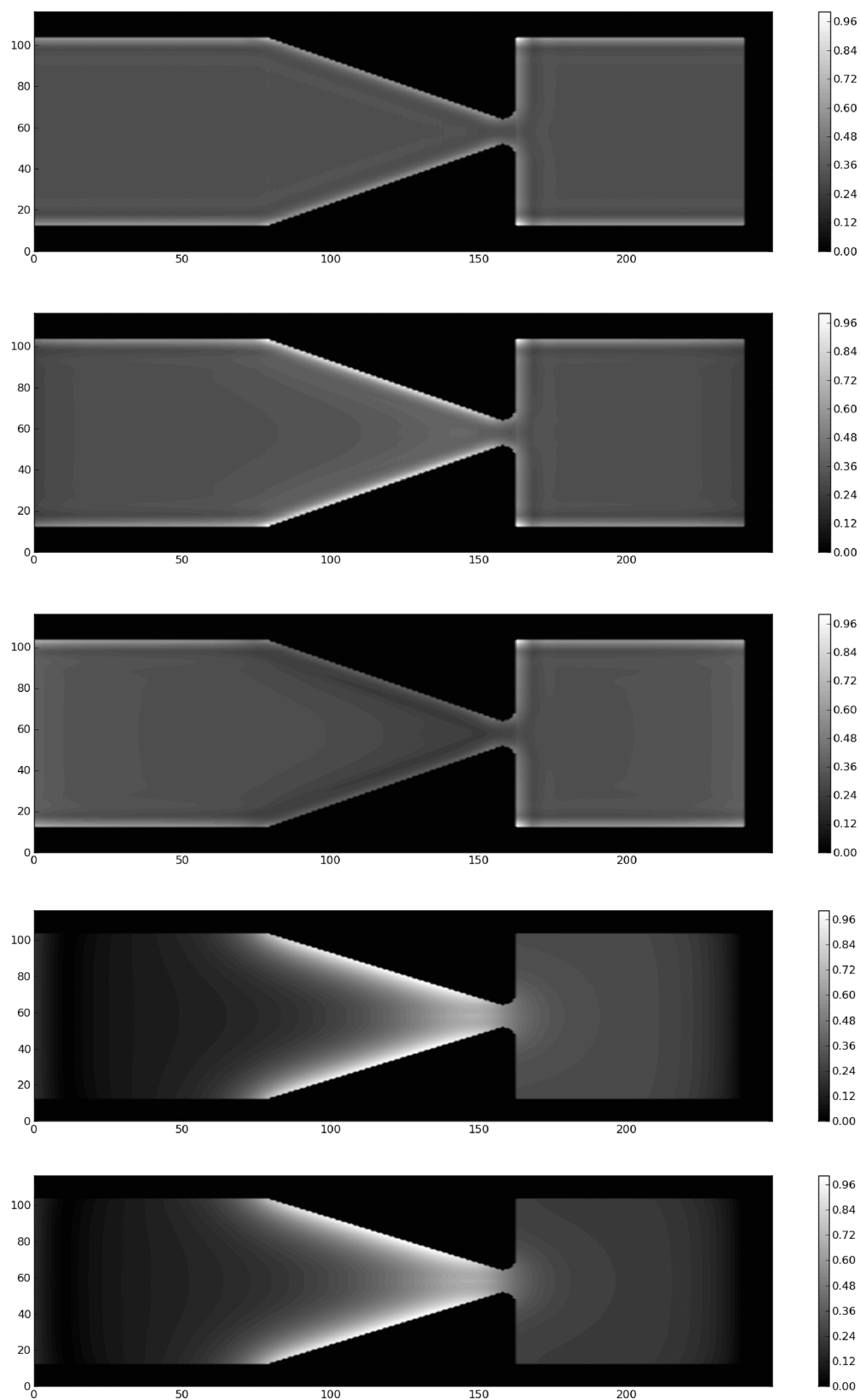


**Figure 6.** (Model C) Contours of scalar fields for the case with  $\Sigma = -0.002$  and voltage  $0.3k_B T$ . (Top to bottom) Density of the neutral species, density of counterions, density of co-ions, and electrostatic potential. The lowest panel is the electrostatic potential for the equivalent system without hard sphere forces.

conductivity near the orifice that would produce asymmetry in fluxes of counterions and co-ions.<sup>48</sup> In this context, a third cause of rectification could be due to local charge accumulation in the

wedge pore region, that is, an imperfect Donnan compensation of surface charges. It is thus interesting to look at the highly nontrivial distribution of neutral and charged species, as

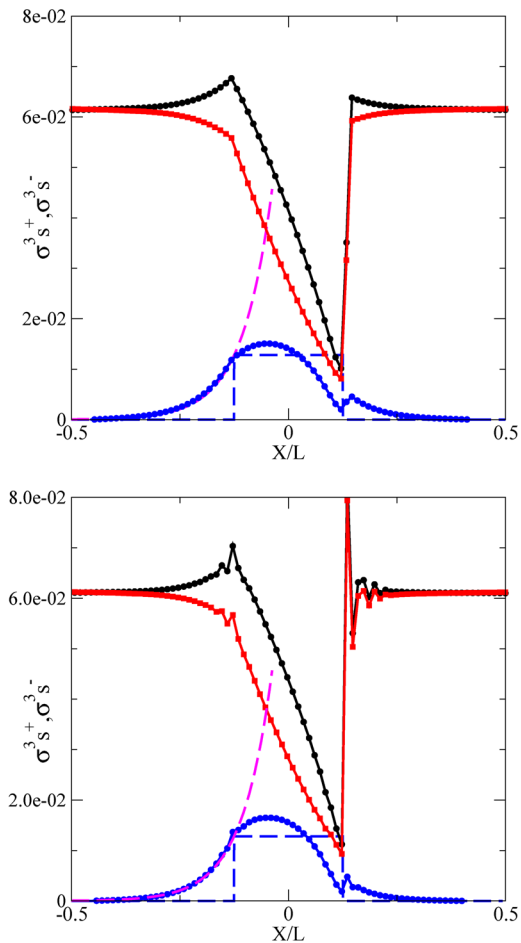


**Figure 7.** (Model C) Transversally averaged density profiles of the two ionic species with (upper panel) and without (lower panel) HS collisions. The black curve represents the counterion profile  $s^+(x)$ , the red curve represents the co-ion profile  $s^-$ , and the blue curve represents their difference (the local charge). The latter has to be compared with the surface charge density profile (blue stepwise dashed curve). Finally, as a guide to the eye, the exponential decay with a characteristic Debye length,  $\lambda_D$ , is reported as a violet dashed curve.

displayed in Figure 6 for the contour plots for the density of species in model C for a surface charge of  $\Sigma = -0.002$ . The plots show that the several walls present in the wedge geometry strongly modulate the density profiles of each species as the effect of layering and that this layering overlaps with the double-layer organization. We further notice that the concave corners act as strong accumulation points for the species, similarly to what was shown some time ago by Dietrich and co-workers.<sup>47</sup> The reason for the accumulations is completely entropic and is such that the concave corners effectively attract particles whereas convex corners exert repulsive forces. Figure 6 reports the electric potential in the same geometry at zero and finite packing fractions, and surprisingly, the self-consistent solution for the potential does not depend sensibly on the presence of hard sphere interactions.

We next evaluate the charge count along the  $x$  direction and in the absence of external voltage for model C. The charge count is defined as  $s^\pm(x) \equiv (1/S) \int n^\pm(x, y, z) dy dz$ , where  $S$  is the sectional area, which can be assimilated to the local surface charge of each species. The local excess charge  $\Delta s \equiv (s^+ - s^-)$  should partially compensate for the surface charge in the wedge region. Figure 7 shows several interesting features that strongly

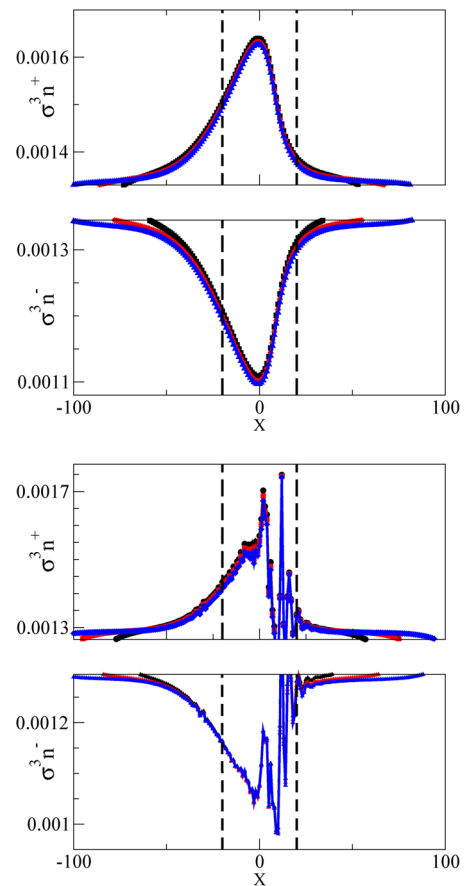


**Figure 8.** (Model C) Density profiles along the channel center line of counterions (upper panel) and co-ions (lower panel) without (left panel) and with (right panel) hard sphere collisions. Profiles for different channel lengths ( $L$ ) are shown: 120 (black), 160 (red), and 200 (blue) in lattice units. Data are for  $\Sigma\sigma^2/e = -0.0032$  and zero voltage. The dashed lines indicate the pore region.

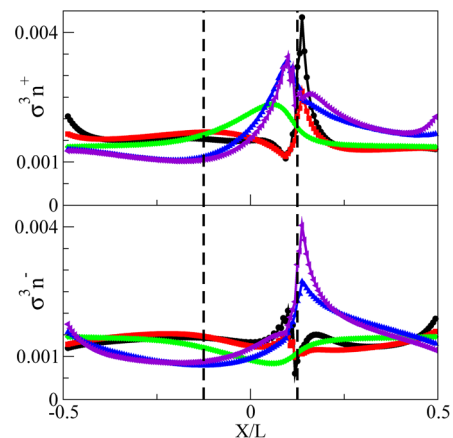


**Figure 9.** (Model C) Density profiles along the channel center line of counterions (upper panel) and co-ions (lower panel) in the presence of hard sphere collisions. Data for voltages  $K/k_B T = -60$  (black),  $-30$  (red),  $0$  (green),  $30$  (blue), and  $60$  (violet) taken at  $\Sigma\sigma^2/e = -0.016$  and  $L/\sigma = 40$ . The dashed lines indicate the limits of the pore region.

depend on the packing fraction. At first, we notice the appearance of oscillations in the profiles induced by the packing effects, which are more pronounced near the narrow exit of the wedge. More importantly, the plots show that the compensation is imperfect and within the wedge region  $\Delta s$  stays around  $-\Sigma$  and

displays strong similarities between the zero and finite packing fraction cases.

Figure 7 reveals how the molecular system departs from the assumption of local charge neutrality often utilized in electrochemical studies. Only away from the pore region the excess charge decays to zero; that is, it restores electroneutrality. The longitudinal decay length is given by  $\lambda_D$  on the side of the larger wedge mouth and shows slightly more complex behavior on the other side. It is an interesting fact that the Debye length controls the longitudinal restoration of electroneutrality, perhaps not completely unexpectedly. However, in practical calculations it is important to determine the finite size effects, such as in the periodic system studied here. Figure 8 shows that channels of size  $L/\lambda_D > 8$  are sufficiently long to show a good convergence of the charge distribution. For our simulations, we have chosen  $L/\sigma = 40$  as the reference channel extensions to obtain satisfactorily converged results.

Once the voltage acts on the system, the charge unbalance modulates the charge organization in highly nontrivial ways. The charge distribution along the channel center line of the wedged geometry is shown in Figure 9 for different voltages. Counterions tend to accumulate and co-ions are depleted in the wedge region for positive voltages. The situation reverses by reversing the bias, and under these conditions, we observe strong charges piling up on the small-mouth side.

In Figure 10, we turn our attention to the mass transport process and display the barycentric velocity profile,  $u_z(x)$ , of the fluid in the  $x$

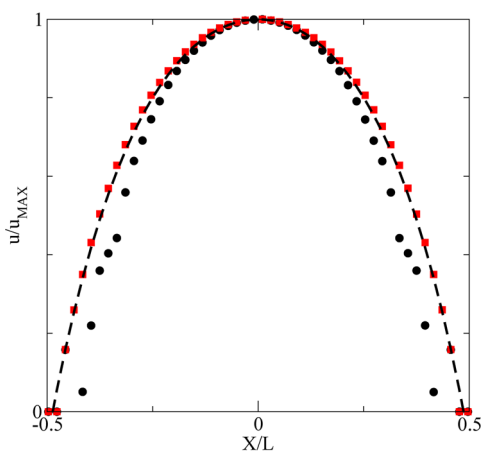


**Figure 10.** (Model A) Barycentric velocity divided by its maximum value. The profile refers to an electrolyte mixture under a voltage  $V/k_B T = 30$  in the absence (squares) and in the presence of HS collisions (circles). The Smoluchowski analytical solution is also displayed (dashed curve).

direction in the case of model A. For the sake of comparison, we also show the prediction of the Smoluchowski analytical formula (eq 11) obtained by calculating the electrostatic potential  $\psi(z)$  within the Debye–Hückel linear approximation. We observe that the agreement between this formula and the results relative to the BGK system is very good, whereas the system with excluded volume interactions displays smaller velocities near the confining walls because of the larger value of the viscosity.

Charge transport in the system is mostly due to ionic conduction rather than electro-osmotic transport. We therefore compute the number of mobile charge carriers in the pore region. As expected for model B, Figure 11 shows symmetric curves upon voltage inversion and rather flat curves. However, for the wedge system, the curves lose their symmetry and become more pronounced with the voltage. Only at the largest value of the

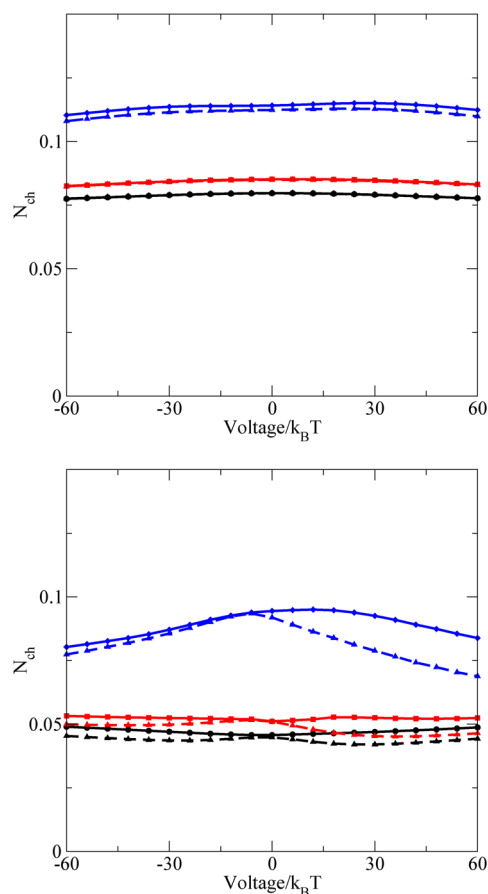


**Figure 11.** (Model C) Number of charge carriers in the pore region  $N_{ch} = \int_{V_{pore}} d^3r [n^+(r) + n^-(r)]$  for models B (upper panel) and C (lower panel). The curves correspond to  $\Sigma\sigma^2/e = -0.0016$  (circles),  $-0.0048$  (squares), and  $-0.016$  (triangles), respectively. Solid lines correspond to the presence of HS collisions whereas the dashed lines do not include HS collisions.

surface charge density does one observe an appreciable deviation between the two channel shapes. In the lower panel of Figure 11, the effect of the wedged geometry determines a nonflat dependence of the number of the mobile charge carriers on the applied voltage. Also, we notice that this number is lower in the presence rather than in the absence of HS collisions because the excluded volume interaction hinders the accumulation of charges in the wedged region. In any case, the undercharging of the pore at nonzero voltage is rather limited ( $<20\%$ ). By the same token, the imperfect neutralization of the wedged region decreases the Drude–Lorentz conductivity for both positive and negative voltages, as compared to the zero voltage condition. The observed modest asymmetry in local charging is also reflected in differences in conductivity for forward versus backward bias. However, rectification usually shows up as a much stronger effect;<sup>44,45</sup> therefore, we exclude the fact that it is due to modulations of the occupation of the wedged region by mobile charge carriers.

To demonstrate the bulklike origin of electrical transport, in Figure 12 we report the numerical data for the electric conductance,  $G$ , for the geometries of models B and C. The simulations provide the ionic current  $I$  and the potential difference  $V$  applied at the ends of the channel, so we computed the conductance according to the equation

$$I = GV \quad (56)$$

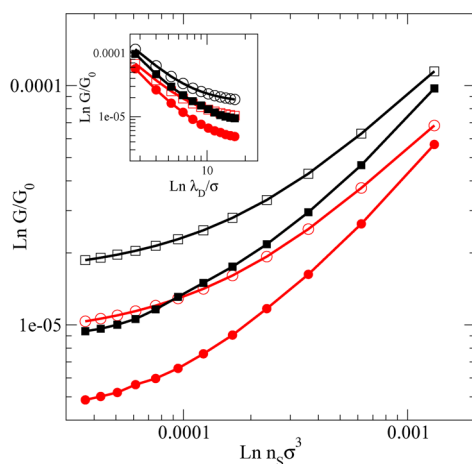


**Figure 12.** Double logarithmic plot of the conductance,  $G$ , vs the number density of carriers  $n_s$  for models B (open symbols) and C (filled symbols) in the presence (circles) and in the absence (squares) of HS collisions. The conductance is reported in units of  $G_0 \equiv e^2/\nu_T\sigma$ . The inset reports the conductance vs the Debye length.

An estimate of  $G$  can be derived using the expression  $G = (\sigma_{el}S)/L$ , where  $S$  is the effective section of the channel, and given the geometry under consideration,  $S/L = 200/80 = 2.5$ .

Figure 13 reports the streaming current, that is, the ionic current arising from a pressure gradient  $\nabla p$  obtained for model B.

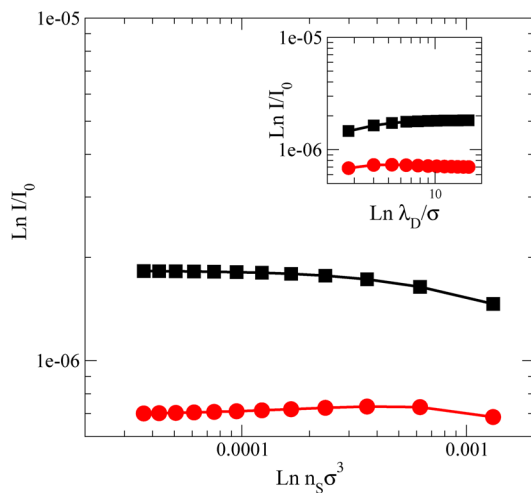


**Figure 13.** Double logarithmic plot of the streaming current vs number density of carriers  $n_s$  for model B in the presence (circles) and in the absence (squares) of HS collisions. The applied force is  $8.33 \times 10^{-7}$  in units of  $\nu_T^2/\sigma$ . The ionic current is reported in units of  $I_0 \equiv e\nu_T/\sigma$ . The inset reports the current vs the Debye length.

The streaming current increases when increasing the Debye length, a behavior that is expected by considering that the ionic current is proportional to the surface potential  $\psi_s$ ,  $I = (\epsilon\psi_s S \nabla p)/\eta_s^3$ , and that the surface potential is roughly proportional to the Debye length. The presence of hard sphere collisions generates streaming currents smaller than those without collisions because of the increased value of the dynamic viscosity.

It should be kept in mind that in order to compare the computed conductances arising from either an electric field or a pressure gradient with the experimentally measured ones the simulated system is the result of a periodic series of charged and uncharged regions of the pore. Nevertheless, the simulation data

are important because they show the intimate nature of conduction. As a matter of fact, as the bulk concentration decreases, the excess surface charges due to the presence of the negatively charged surface of the channel becomes the leading contribution to the conduction mechanism. For very small values of  $n_s$ , the bulk formula  $\sigma_{el} = 2(e^2/\gamma)n_s$  (see eq 35) does not hold and must be modified in order to account for the contribution due to the excess charge arising from the counterions within the pore. By making the hypothesis that electroneutrality is not a global constraint (eq 51) but rather holds locally, we simply replace  $n_s \rightarrow n_s - (\Sigma/eH)$ . The consequence of such replacement is the saturation of the conductance at low values of the electrolyte concentration  $n_s$ , as reproduced qualitatively in Figure 12. Finally, the operational value of  $\lambda_D/\sigma = 2.75$  presently studied corresponds to being relatively far from the saturation regime.

## 6. CONCLUSIONS

We have studied nanometric electro-osmotic flows by means of a self-consistent kinetic description of the phase space distribution functions. The ternary mixture is composed of two oppositely charged species and a third neutral species representing the solvent and is subject to external forces under nonuniform conditions. The short-range interaction between molecules has been modeled by means of a hard sphere repulsion term and treated within the revised Enskog theory. The Coulomb interaction has been treated within the mean field approximation, that is, by disregarding charge-induced correlations.

The presented theory was shown to be consistent with the phenomenological equations of macroscopic electrokinetics, such as the Smoluchowski and Planck–Nernst–Poisson equations. In essence, the approach bridges the microscopic with the hydrodynamic level and allows us to incorporate the inhomogeneity of the ionic solution determined by the presence of the confining surfaces.

To solve the system of equations for the multicomponent system, we have adopted a particular version of the lattice Boltzmann method. We validated the theory and the numerical algorithm by considering the mass and charge transport under the effect of applied electric fields in different channels having nonuniform shapes and nonuniform charging on the wall.

In view of understanding the phenomenon of current rectification as observed in wedged channels having an orifice of nanometric size, we have studied the departures from electroneutrality on the molecular scale. We have found that electroneutrality is restored along the longitudinal direction within a Debye length. In addition, we observed mild undercharging of the wedged region at a finite applied voltage. The asymmetry of the curves for positive versus negative voltage is modest, ruling out the possibility that this is at the origin of current rectification.

Besides the geometries presented here, the proposed methodology can be applied to a larger class of problems in electrofluidics. For instance, it is possible to include semipermeable membranes, that is, channels impermeable to one type of ion and to the solvent. Other kinds of confining walls can be analyzed, such as chemically heterogeneous surfaces. A more comprehensive investigation of the role of differences in the mass and size of the particles is currently underway.

## AUTHOR INFORMATION

### Corresponding Author

\*E-mail: umberto.marinibettolo@unicam.it; simone.melchionna@roma1.infn.it

## Notes

The authors declare no competing financial interest.

## ACKNOWLEDGMENTS

We are grateful to Z. Siwy, C. Holm, C. Pierleoni, and J.-P. Hansen for illuminating discussions.

## REFERENCES

- (1) Eijkel, J. C. T.; van den Berg, A. Nanofluidics: what is it and what can we expect from it? *Microfluid. Nanofluid.* **2005**, *1*, 249.
- (2) Sparreboom, W.; van den Berg, A.; Eijkel, J. C. T. Principles and applications of nanofluidic transport. *Nat. Nanotechnol.* **2009**, *4*, 713.
- (3) Bocquet, L.; Charlaix, E. Nanofluidics, from bulk to interfaces. *Chem. Soc. Rev.* **2009**, *39*, 1073.
- (4) Schoch, R. B.; Han, J.; Renaud, P. Transport phenomena in nanofluidics. *Rev. Mod. Phys.* **2008**, *80*, 839.
- (5) Bruus, H., *Theoretical Microfluidics*; Oxford University Press: New York, 2008.
- (6) Masliyah, J. H.; Bhattacharjee, S. *Electrokinetic and Colloid Transport Phenomena*; John Wiley and Sons: New York, 2006.
- (7) Kirby, B. J. *Micro and Nanoscale Fluid Mechanics: Transport in Microfluidic Devices*; Cambridge University Press: New York, 2010.
- (8) Mukhopadhyay, R. Diving into droplets. *Anal. Chem.* **2006**, *78*, 7379.
- (9) Kontturi, K. Murtoimäki, L. Manzanares, J. A. *Ionic Transport Processes: In Electrochemistry and Membrane Science*; Oxford University Press: New York, 2008.
- (10) Quiao, R.; Aluru, N. R. Ion concentrations and velocity profiles in nanochannel electroosmotic flows. *J. Chem. Phys.* **2003**, *118*, 4692.
- (11) Nilson, R. H.; Griffiths, S. K. Influence of atomistic physics on electro-osmotic flow: an analysis based on density functional theory. *J. Chem. Phys.* **2006**, *125*, 164510.
- (12) Eisenberg, B.; Hyon, Y.; Liu, C. Energy variational analysis of ions in water and channels: field theory for primitive models of complex ionic fluids. *J. Chem. Phys.* **2010**, *133*, 104104.
- (13) Zhu, W.; Singer, S. J.; Zheng, Z.; Conlisk, A. T. Electro-osmotic flow of a model electrolyte. *Phys. Rev. E* **2005**, *71*, 041501.
- (14) Press, W. H. et al. *Numerical Recipes in C: The Art of Scientific Computing*; Cambridge University Press: New York, 2007.
- (15) Karniadakis, G.; Beskok, A.; Aluru, N. R. *Microflows and Nanoflows: Fundamentals and Simulation*; Springer: Berlin, 2005.
- (16) Tian, R.; Li, B.; Kwok, D. Y. *Lattice Boltzmann Simulation of Electroosmotic Flows in Micro- and Nanochannels*; Proceedings of the 2004 International Conference on MEMS, NANO and Smart Systems.
- (17) Guo, Z.; Zhao, T. S.; Shi, Y. A lattice Boltzmann algorithm for electro-osmotic flows in microfluidic devices. *J. Chem. Phys.* **2005**, *122*.
- (18) Wang, J.; Wang, M.; Li, Z. Lattice Poisson–Boltzmann simulations of electro-osmotic flows in microchannels. *J. Colloid Interface Sci.* **2006**, *296*, 729.
- (19) Wang, M.; Kang, Q. Modeling electrokinetic flows in microchannels using coupled lattice Boltzmann methods. *J. Comput. Phys.* **2010**, *229*, 728.
- (20) Melchionna, S.; Succi, S. Electrorheology in nanopores via lattice Boltzmann simulation. *J. Chem. Phys.* **2004**, *120*, 4492.
- (21) Melchionna, S.; Marini Bettolo Marconi, U. Electro-osmotic flows under nanoconfinement: a self-consistent approach. *Europhys. Lett.* **2011**, *95*, 44002.
- (22) van Beijeren, H.; Ernst, M. H. The modified Enskog equation. *Physica A* **1973**, *68*, 437.
- (23) Marini Bettolo Marconi, U.; Melchionna, S. Phase-space approach to dynamical density functional theory. *J. Chem. Phys.* **2007**, *126*, 184109.
- (24) Marini Bettolo Marconi, U.; Melchionna, S. Dynamic density functional theory versus kinetic theory of simple fluids. *J. Phys.: Condens. Matter* **2010**, *22*, 364110.
- (25) Rauscher, M. DDFT for Brownian particles and hydrodynamics. *J. Phys.: Condens. Matter* **2010**, *22*, 364109.
- (26) Dufty, J. W.; Santos, A.; Brey, J. Practical kinetic model for hard sphere dynamics. *Phys. Rev. Lett.* **1996**, *77*, 1270.
- (27) Santos, A.; Montanero, J. M.; Dufty, J. W.; Brey, J. J. Kinetic model for the hard-sphere fluid and solid. *Phys. Rev. E* **1998**, *57*, 1644.
- (28) Succi, S. *The Lattice Boltzmann Equation for Fluid Dynamics and Beyond*. Oxford University Press: New York, 2001.
- (29) Benzi, R.; Succi, S.; Vergassola, M. The lattice Boltzmann equation: theory and applications. *Phys. Rep.* **1992**, *222*, 145.
- (30) Melchionna, S.; Marini Bettolo Marconi, U. Lattice Boltzmann method for inhomogeneous fluids. *Europhys. Lett.* **2008**, *81*, 34001.
- (31) Marini Bettolo Marconi, U.; Melchionna, S. Kinetic theory of correlated fluids: from dynamic density functional to lattice Boltzmann methods. *J. Chem. Phys.* **2009**, *131*, 014105.
- (32) Marini Bettolo Marconi, U.; Melchionna, S. Multicomponent diffusion in nanosystems. *J. Chem. Phys.* **2011**, *135*, 044104.
- (33) The polarizability of the medium could be accounted for by endowing the neutral component of the mixture with a permanent dipole as proposed by Olesky, A.; Hansen, J.-P. *J. Chem. Phys.* **2010**, *132*, 204702.
- (34) Bhatnagar, P. L.; Gross, E. P.; Krook, M. A model for collision processes in gases. I. Small amplitude processes in charged and neutral one-component systems. *Phys. Rev.* **1954**, *94*, 511.
- (35) Marini Bettolo Marconi, U.; Melchionna, S. Dynamics of fluid mixtures in nanospaces. *J. Chem. Phys.* **2011**, *134*, 064118.
- (36) Melchionna, S.; Marini Bettolo Marconi, U. Stabilized lattice Boltzmann-Enskog method for compressible flows and its application to one and two-component fluids in nanochannels. *Phys. Rev. E* **2012**, *85*, 036707.
- (37) Fischer, J.; Methfessel, M. Born-Green-Yvon approach to the local densities of a fluid at interfaces. *Phys. Rev. A* **1980**, *22*, 2836.
- (38) Boublik, T. Hard-sphere equation of state. *J. Chem. Phys.* **1970**, *53*, 471.
- (39) Mansoori, G. A.; Carnahan, N. F.; Starling, K. E.; Leland, T. W. Equilibrium thermodynamic properties of the mixture of hard spheres. *J. Chem. Phys.* **1971**, *54*, 1523.
- (40) Joly, L.; Ybert, C.; Trizac, E.; Bocquet, L. Liquid friction on charged surfaces: from hydrodynamic slippage to electrokinetics. *J. Chem. Phys.* **2006**, *125*, 204716.
- (41) Corry, B.; Kuyucak, S.; Chung, S.-H. Tests of continuum theories as models of ion channels. II. Poisson-Nernst-Planck theory versus Brownian dynamics. *Biophys. J.* **2000**, *78*, 2364.
- (42) Kilic, M. S.; Bazant, M. Z.; Ajdari, A. Steric effects in the dynamics of electrolytes at large applied voltages. I. Double-layer charging. *Phys. Rev. E* **2007**, *75*, 021503.
- (43) Frenkel, D.; Smit, B. *Understanding Molecular Simulation: From Algorithms to Applications*; Academic Press: San Diego, CA, 2002.
- (44) Powell, M. R.; Sa, N.; Davenport, M.; Healy, K.; Vlassioulis, I.; Letant, S. E.; Baker, L. A.; Siwy, Z. S. Noise properties of rectifying nanopores. *J. Phys. Chem. C* **2011**, *115*, 8775.
- (45) Siwy, Z.; Fulinski, A. Fabrication of a synthetic nanopore ion pump. *Phys. Rev. Lett.* **2002**, *89*, 198103.
- (46) Cervera, J.; Schiedt, B.; Ramirez, P. A Poisson/Nernst-Planck model for ionic transport through synthetic conical nanopores. *Europhys. Lett.* **2005**, *71*, 35.
- (47) Bryk, P.; Roth, R.; Schoen, M.; Dietrich, S. Depletion potentials near geometrically structured substrates. *Europhys. Lett.* **2003**, *63*, 233.
- (48) Woermann, D. Electrochemical transport properties of a cone-shaped nanopore: revisited. *Phys. Chem. Chem. Phys.* **2004**, *6*, 3130.